TECHNICAL ARTICLE

Building Orientation and Heat Treatments Effect on the Pseudoelastic Properties of NiTi Produced by LPBF

G. Carlucci[1] · L. Patriarca[1] · A. G. Demir[1] · J. N. Lemke[2] · A. Coda[2] ·
B. Previtali[1] · R. Casati[1]

Abstract NiTi dominates the market of shape memory materials due to its optimal combination of mechanical, functional, and biocompatibility properties, which enabled its use for several applications, in particular for the biomedical and the aerospace sectors. However, due to its poor machinability, NiTi is a challenging material from the manufacturing standpoint. Therefore, in the last years, researchers have focused on the production of NiTi components by additive manufacturing processes, which also enable the manufacturing of complex shape parts that cannot be produced with conventional methods. The aim of this study is to provide insights on the optimization of the functional performances of NiTi produced by Laser Powder Bed Fusion, leveraging on the building orientation and post-processing heat treatments. Uniaxial mechanical tests have been performed in tension and compression, and the influence of heat treatments and building orientation on the mechanical behavior of pseudoelastic NiTi has been evaluated. Different heat treatment schedules have been evaluated, leading to transformation strains up to 2.7% in tension and 4.6% in compression. This study confirms that Laser Powder Bed Fusion is a promising additive manufacturing technology for the production of net-shape and near defect-free NiTi components, exhibiting remarkable functional properties.

✉ L. Patriarca
luca.patriarca@polimi.it

1 Department of Mechanical Engineering, Politecnico di Milano, Via La Masa 1, 20156 Milan, Italy

2 SAES Getters S.p.A., Viale Italia 77, 20045 Lainate, Italy

Introduction

Shape memory alloys (SMAs) exhibit unique functional properties such as the shape memory, the pseudoelasticity (or superelasticity) [1], and the elasto-caloric effect [2, 3]. These properties make the SMAs suitable for applications in the biomedical, aerospace, civil, and automotive sectors [4–6]. Among the different SMAs, NiTi is the most widely studied, due to its superior transformation strain, mechanical properties, and biocompatibility [7, 8]. The capability of NiTi to recover its original shape is determined by a reversible phase transformation between the cubic B2 austenitic phase and the monoclinic B19' martensitic phase [9, 10]. In spite of the excellent functional properties, one of the main drawbacks of NiTi is the poor machinability that limits to some extent its fields of application [11, 12]. Given this context, the possibility to realize NiTi components by additive manufacturing (AM) gathered an increasing interest [13–18], since it allows producing, layer-by-layer, net-shape 3D objects, avoiding the typical constraints of the conventional melting and forming methods [19].

The AM functional materials that are able to change their shape providing an external stimulus (e.g., mechanical, thermal, magnetic or electric) is commonly referred to as "4D printing" [20]. One of the most widespread AM techniques for metals is the Laser Powder Bed Fusion (LPBF), which uses a high-power laser beam to melt locally a layer-wise deposited metallic powder. The recent literature is rich of research works focused on the 4D printing of NiTi, in particular using LPBF [21–33], showing the interest of the scientific community on this topic, as also evidenced by a substantial number of reviews [13, 14, 34].

🖉 Springer

The production of NiTi components by LPBF brings up new challenges such as the precise control of the chemical composition to obtain the desired functional properties in final parts [21]. Small variations in the Ni/Ti ratio cause relevant changes in the characteristic transformation temperatures of the material, and therefore in its mechanical and functional performances [35]. In particular, nickel is more volatile than titanium and tends to evaporate under the laser radiation [36, 37]. Consequently, a proper optimization of the process parameters is of paramount importance to achieve fully dense parts with sound functional properties [38]. Biffi et al. [33] reported that with an energy density within the interval $63 \div 160$ J/mm^3, it was possible to obtain high values of relative density for NiTi specimens produced by LPBF. Saedi et al. [21] fabricated NiTi samples with good pseudoelastic performance with an energy density of 222.2 J/mm^3. Moghaddam et al. [26] demonstrated the potential of LPBF to tune the functional behavior of NiTi by a proper calibration of the process parameters. For a sample manufactured with an energy density of 83.33 J/mm^3, they reported a strain recovery of 5.62% without any post-process heat treatment.

Even though acceptable functional behavior has been reported also for the as-built NiTi specimens [26], heat treatments provide a further possibility to tailor and enhance the NiTi functional properties [22, 31, 33, 39]. In this regard, Haberland et al. [39] reported the formation of a high amount of finely dispersed Ni_4Ti_3 precipitates after solution annealing followed by aging at 350 °C. These precipitates are considered to play a fundamental role in the functional behavior of the material, since they can act as nucleation sites for the martensite. However, as a drawback, the precipitates are reported to embrittle the metal matrix and prolonged aging can lead to their coarsening and, consequently, reduced pseudoelastic performances. Saedi et al. [22] studied the effect of aging treatments on the functional properties of $Ni_{50.8}Ti_{49.2}$ (at.%) alloy produced by LPBF. The authors reported that, after solution annealing at 950 °C followed by aging at 350 °C, the material exhibited good pseudoelastic behavior, i.e., 5.5% strain recovery with 0.3% unrecoverable strain. They also observed a stabilized strain recovery of 4.2% following ten loading cycles. In another study, Saedi et al. [31] obtained a strain recovery of 5.5% after aging at 600 °C, without solution annealing. Biffi et al. [33] obtained a full recoverable strain of 6% after heat-treating additively manufactured NiTi at 500 °C.

It should be noted that the former cited studies focused on the NiTi testing under pure compression loads. This is due to the fact that NiTi has scarce LPBF processability and parts without a significant amount of porosity and defects, which are detrimental for the tensile properties, can be hardly produced [14]. Only recently, research studies showing tensile properties of NiTi produced by LPBF have been published [40–42]. Nematollahi et al. [40] reported a strain recovery of 5.31% in tension for the as-built dog-bone NiTi specimen manufactured by LPBF. Lu et al. [41] obtained stable tensile recovery strain up to 3.74% during cyclic tests of aged NiTi specimens. They attributed this to the saturation of the dislocations formed during the cycles, thanks to the dislocation pile-up around the Ni_4Ti_3 nanoprecipitates. More recently, Xue et al. [42] obtained tensile pseudoelasticity values up to 6% in the as-built state by tailoring process parameters and by a strict control of the oxygen content within the building chamber. We also note that other additive manufacturing technologies applied to NiTi have shown promising tensile properties, such as Electron Beam Freeform [43] and Wire Arc Manufacturing [44].

It becomes evident that, for a widespread industrial application, more efforts are required to guarantee excellent tensile properties of NiTi produced by LPBF. For this reason, this study aims to further investigate the tensile behavior of NiTi produced by LPBF focusing on two loading directions—namely vertical and horizontal—with respect to the building orientation. In this regard, one of the most important characteristics of the AM process is the mechanical anisotropy, which arises from the formation of columnar grains, crystallographic texture, and "fish-scale" structure typical of the as-printed material [45]. This is of particular importance considering that, for NiTi alloys, the transformation strain associated with the austenitic-martensitic transformation is strongly affected by the crystallographic orientation of grains [24, 40, 46–48]. Nematollahi et al. [40] investigated for the first time the effects of the building orientation on the microstructure and the functional properties of 3D printed NiTi. The samples with a prevalent $< 001 >$ orientation along the loading direction showed a tensile strain recovery of 2.87%, while a prevalent $< 110 >$ orientation resulted in a strain recovery of 5.31%.

The microstructure of NiTi might also determine a strong heterogeneous martensitic transformation which does not occur with the same extent across the whole volume of the specimen, while it can be locally favored for grains having a more suitable orientation. Therefore, in the last years, it has become common practice the use of Digital Image Correlation (DIC) to collect full field strain maps and to locally quantify the degree of phase transformation and recoverable strains [40, 49]. In the present study, DIC strain measurements were carried out to study the macro- and micro-transformation strains providing fundamental insights into the transformation behavior of the present LPBF NiTi alloy.

The literature review reported in the previous paragraphs shows that more efforts are necessary for a

complete understanding of the combined effect of building orientation and heat treatments on the functional behavior of additively manufactured NiTi and for its full exploitation in real applications. Moreover, few attempts to investigate the tensile behavior of additively manufactured NiTi have been performed so far. In this regard, we carried out an experimental campaign which involved the design of different heat treatment routes and the tensile/compression testing of NiTi samples produced by LPBF along different orientations. Uniaxial mechanical tests have been performed both in tension and compression and DIC has been used to investigate the transformation strain heterogeneities exhibited by the manufactured specimens.

Materials and Methods

Powder and Specimen Manufacturing

NiTi gas-atomized powder with a particle size distribution between 15 and 45 μm was provided by SAES Getters. The nominal composition of the powder was 50.8 at.% Ni and 49.2 at.% Ti. All the specimens were produced by means of a Renishaw AM250 industrial LPBF system, equipped with a 200 W single mode fiber laser (R4 from SPI, Southampton, UK) and an optical chain which provides a 75 μm beam diameter in the focal position. A Reduced Built Volume (RBV) platform was used for this work, so that the build chamber was limited to $78 \times 78 \times 50$ mm^3. The specimens were obtained using a meander scanning strategy. To minimize oxygen pickup, the process was carried out under a controlled argon flow.

The selection of processing condition was performed by varying the process parameters to obtain a proper energy density and specimens with high relative density. Suitable process parameters were found to be a power of 150 W, an exposure time of 60 μs, a point distance of 45 μm, and a hatch distance of 45 μm, leading to a relative density of 99.3% and crack-free specimens. Tensile tests were performed using dog-bone specimens, with external dimensions of 23 mm $\times$ 6 mm $\times$ 1.5 mm (Fig. 1a) and cross section of 3×1.5 mm^2, whereas compressive tests were carried out on solid cuboidal specimens, with dimensions of 8 mm $\times$ 8 mm $\times$ 16 mm (Fig. 1b). Two batches of tensile specimens were printed, with two different loading axis orientations, namely *vertical* (i.e., loading direction parallel to the building direction) and *horizontal* (i.e., loading direction orthogonal to the building direction). The compression specimens, instead, were manufactured only in the vertical direction. Figure 1 shows the sizes of the specimens, along with their orientation on the build platform.

Specimen Preparation and Experimental Setup

Samples for metallographic analysis were grinded with sandpapers down to 2500 grit and polished with diamond pastes with particle size in the range of 6 to 1 μm. The samples for Electron Backscattered Diffraction (EBSD) analyses were finally polished by colloidal silica. The tensile specimens were polished on both sides to reach a thickness of 1 mm. Moreover, the lateral sides of the specimens were machined to improve surface quality.

The phase composition of the materials was studied by means of X-ray diffraction (XRD) analyses using a Rigaku SmartLab SE X-ray diffractometer with Cu K_α radiation ($\lambda = 0.154$nm). XRD patterns were collected at 40 kV and 40 mA with Bragg–Brentano geometry in a 2θ range of $10 \div 120°$ with a step size of 0.02° and a speed of 1°/min. Pattern indexing and phase identification were performed with the aid of the software SmartLab Studio II.

Microstructural analyses were carried out by a Nikon Eclipse LV150NL optical microscope (OM) and a Zeiss Sigma 500 field emission scanning electron microscope (FE-SEM) equipped with an EBSD detector. To perform OM and FE-SEM analyses, samples were etched with a solution composed of 5 mL of hydrofluoric acid (HF), 20 mL of nitric acid (HNO$_3$), and 25 mL of water, according to what reported in [50]. Water was used instead of acetic acid (CH$_3$COOH) to avoid pitting and overetching. The software used to perform EBSD analyses and to elaborate the acquired data were AZtec and Tango, respectively, developed by Oxford Instruments. For all the analyses, tilt angle and accelerating voltage were set at 70° and 20 kV, respectively, while step size was set differently depending on the magnification (i.e., 1.3 μm for 250 $\times$ and 0.04 μm for 10 000 $\times$).

Tensile tests were performed on dog-bone specimens by means of a DEBEN Microtest dual screw testing stage, which can sustain a maximum load of 5 kN. Compressive tests on solid cuboidal specimens were performed using an MTS Alliance RF/150 electromechanical testing machine. Both the tensile and compressive tests were carried out at room temperature in displacement control (i.e., 0.8 mm/min in compression and 0.3 mm/min in tension).

For all the mechanical tests, DIC was used to measure local strain fields during specimen deformation. A thin layer of white and black paints was sprayed on the specimens by means of an Iwata airbrush which enabled to produce an appropriate speckle pattern for DIC measurements. The field of view for the real-time DIC measurements was approximately 6 mm $\times$ 12 mm for the compressive specimens and 3 mm $\times$ 9 mm for the tensile specimens. The images were continuously acquired during loading by a high-resolution Allied Vision Manta CCD camera, while the specimen's surface was illuminated by

Fig. 1 Geometry and the as-built appearance of **a** the tensile specimens and **b** the compressive specimens. All dimensions are in mm
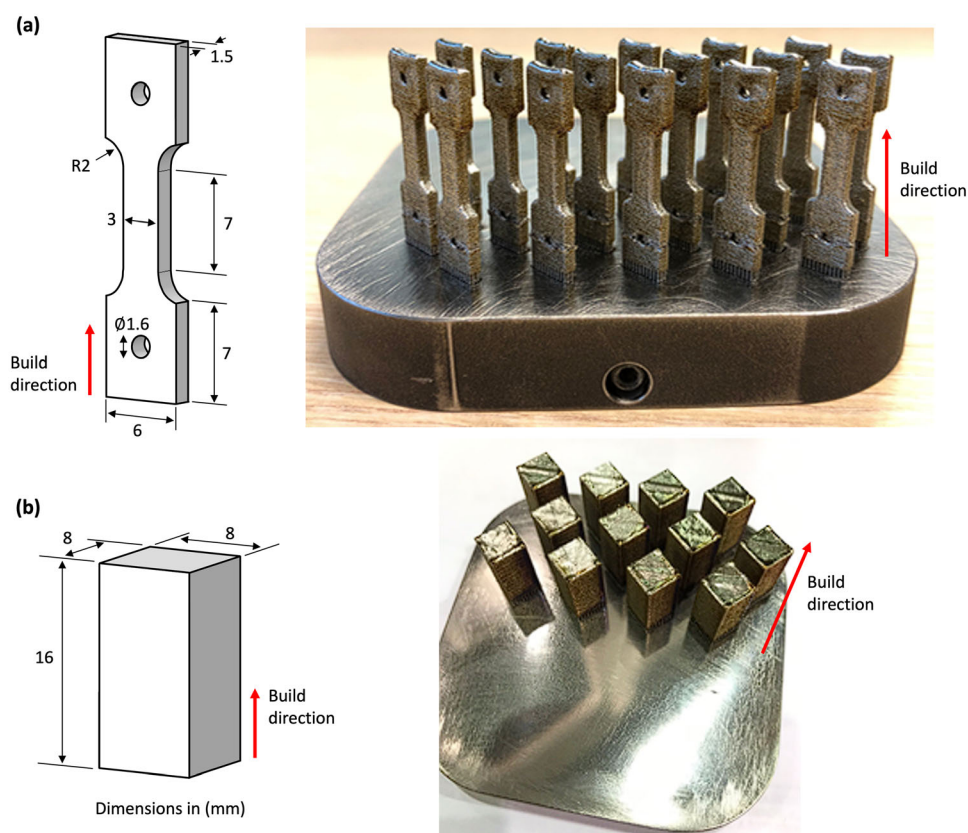
two LED lights. Successively, all the acquired data were analyzed with the VIC-2D DIC software.

The measured DIC strain fields were used to produce two types of strain measurements. At the macro-scale, an averaged axial strain (labeled as *global strain*) represents the bulk mechanical behavior of the specimen. This strain measurement is similar to the strain that can be obtained by an extensometer. On the other side, local strains were also pinpointed in the regions of the specimens' surfaces that displayed the largest deformations (labeled as *local strains*). This type of measurement enabled the characterization of the maximum transformation strain for all the conditions investigated in the present study (i.e., heat treatments, loading orientation, and compression/tension).

Heat Treatments

The influence of heat treatments on the mechanical properties of the material was evaluated by implementing different heat treatment routes, including solution annealing and aging. Aging was performed starting from samples both in the as-built condition and after solution annealing (SA) at 850 °C for 30 min, followed by water quenching (WQ). Aging temperatures were set at 400 °C and 450 °C for 15 min and 500 °C for one hour, respectively. The details are reported in Table 1. Heat treatments were carried out in electrical resistance furnaces Carbolite HRF 7/22D for aging and Carbolite 3216 GPC 12/36 for solution annealing.

The effect of the heat treatments on the transformation temperatures of NiTi was evaluated by means of DSC analyses using a DSC-Q2000 by TA instruments. After evaluating reproducibility on sacrificial test pieces, measurements were performed on $20 \div 100$ mg samples, cycling from 150 to -150 °C and back, with a thermal rate of 10 °C/min. The analyses were performed on powder and bulk samples. The transformation temperatures were evaluated by means of the tangent method, measuring the onset and the offset of the transformation peaks.

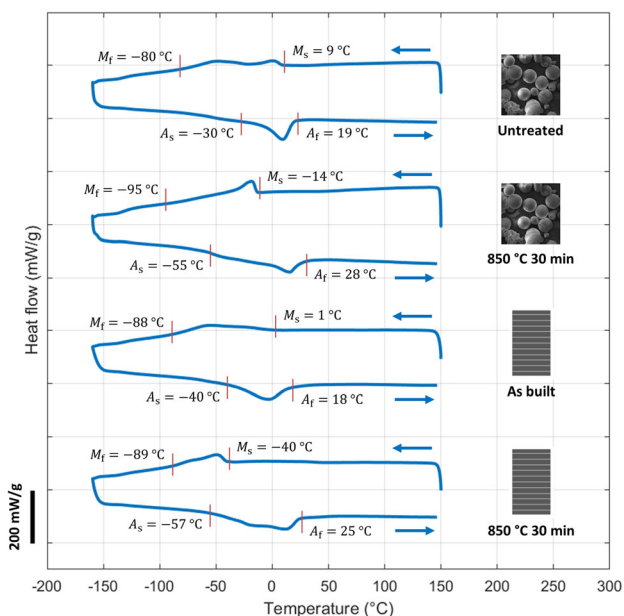**Table 1** Heat treatment schedules adopted for the experiments

Heat treatment	Temperature	Time
Aging	400 °C	15 min
Aging	450 °C	15 min
Aging	500 °C	1 h
SA + WQ	850 °C	30 min
SA + WQ + aging	850 °C + 400 °C	30 min + 15 min
SA + WQ + aging	850 °C + 450 °C	30 min + 15 min

Results and Discussion

Effect of the LPBF Process on the transformation temperatures

The results of the DSC analyses performed on the powder and on the printed specimens are reported in **Fig. 2**. The transformation temperatures are highlighted by the red vertical lines. The untreated powder exhibits a double transformation peak on cooling, which can be likely justified in two ways. Firstly, the presence of residual stresses due to the rapid cooling rate at which the powder was subjected during the atomization process can induce the formation of the R-phase as an intermediate step in the transformation of austenite into martensite [28]. Secondly, local chemical inhomogeneity (micro-segregations) within the microstructure can induce some regions to transform before others, making the transformation to occur in different steps [28, 51]. A confirmation of these two explanations could be the fact that the solution-treated powder exhibits only one transformation peak on cooling, a smaller hysteresis and a slight shift of transformation to higher temperatures, since solution annealing allows to alleviate the residual stresses and to provide chemical homogenization.

For what concerns the bulk samples, the DSC curve of the as-built condition shows a trend that is similar to that of the untreated powder. Solution annealing has an important effect on the transformation temperatures also for the printed specimen. The A_f temperature slightly increases from 18 to 25 °C after solution annealing. A more pronounced effect can be seen on the forward transformation in terms of shift in the M_s temperature, which is reduced from 1 to − 40 °C after the heat treatment. It is assumed that the macroscopic residual stresses induced by LPBF are released upon solution treatment, stabilizing the parent phase. Furthermore, the repeated thermal cycles during LPBF processing can have an effect similar to that of aging, causing precipitation of Ni_4Ti_3 precursors and inducing a double stage transformation that involves the R-phase transformation [52]. In fact, the as-built specimen exhibits a broader peak related to the martensitic transformation, while after solution annealing, the peak appears to be sharper. This can be an indication of the capability of solution annealing to reduce chemical and microstructural inhomogeneities, dislocation density, and residual stresses [53]. The decreasing in M_s temperature after solution annealing can be also justified considering that, during the heat treatment, Ni-rich second phases are dissolved in the austenitic matrix, thus increasing the nickel content [54]. The increase of nickel content in the matrix is well known to reduce the M_s temperature [35].

Phase Identification

XRD analysis was performed both on powder and the as-built samples. The effect of solution annealing and aging was investigated as well. The diffractograms are shown in Fig. 3. The results indicate that both the untreated powder and the as-built sample are mainly composed by fully B2 austenitic structure. Regarding the solution-treated sample,

Fig. 2 DSC curves of the NiTi powder and printed samples in different conditions
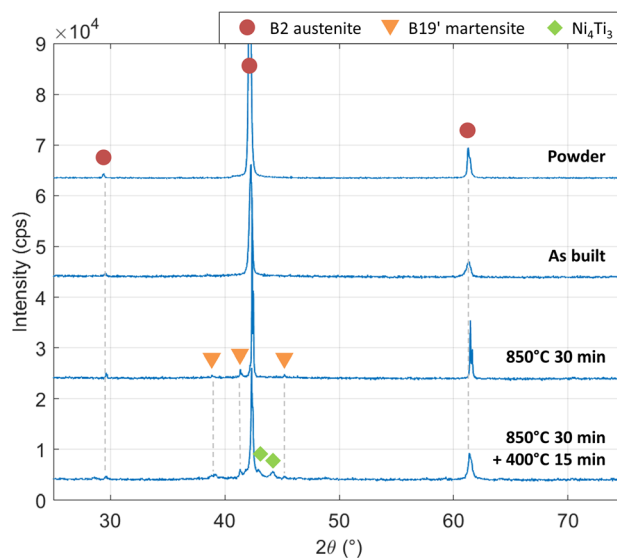
Fig. 3 From the top to the bottom: XRD diffractograms of the untreated $Ni_{50.8}Ti$ powder and the as-built material, after solution annealing at 850 °C and after solution annealing at 850 °C followed by aging at 400 °C

small peaks belonging to the B19' martensitic phase also arise, suggesting a minor amount of martensite. In addition, the pattern of the solution-treated and aged sample shows peaks of the Ni_4Ti_3 precipitates formed during the heat treatment at 400 °C.

Microstructure

A SEM micrograph of the gas-atomized powder used for this work is reported in Fig. 4a. The powder particles have a size between 15 and 45 μm. An optical micrograph performed on the as-built material is reported in Fig. 4b. The microstructure is characterized by large columnar grains that grew epitaxially through the layers. The key feature behind this kind of growth is the partial re-melting of the previous solidified layer, which induces the grains to grow with a crystallographic orientation similar to that of the grains of the already solidified layer [40]. The grains which are preferentially oriented along the direction of the temperature gradient tend to grow at a higher rate, at the expenses of the less favorably oriented neighboring grains.

The melt pools are not visible in the optical micrographs, but they can be clearly seen in the SEM micrograph in Fig. 4c. The columnar grains that grew through the different layers are also noticeable. At higher magnification, fine solidification cells are revealed, as shown in Fig. 4d. The formation of this fine microstructure can be ascribed to the high cooling rate and severe thermal gradients, which occur in LPBF.

The EBSD maps in Fig. 5 show the grain structure of the central area of the as-built specimen. The grains grew for hundreds of micrometers along the building direction (in this case identified by the y axis). The phase map reported in Fig. 5 suggests that the material is in a completely austenitic state. However, at higher magnification (Fig. 6), martensite is visible at grain boundaries. The formation of martensite can be ascribed to heterogeneities in the composition or to the presence of residual stresses between adjacent grains.

The kernel average misorientation (KAM) map of the austenitic grains is also reported in Fig. 6, showing high misorientation level next to the martensite areas. Such local strains could be responsible for the formation of stress-induced martensite (SIM).

Compression Tests

Compression specimens were tested with the loading direction parallel to the building direction. The corresponding curves are shown in Fig. 7a, where the labels indicate the heat treatment performed on the specimen at which each curve corresponds. For all the tests, the critical stress to induce the martensitic transformation (σ_{PE}) and the extent of pseudoelastic recoverable strain (ε_{PE}) were evaluated according to the scheme in Fig. 7b. The critical stress σ_{PE} was evaluated as the onset of the stress–strain curve corresponding to a deviation from the initial linear elastic behavior of 0.2%, while the recoverable strain ε_{PE} was calculated by subtracting the maximum strain in correspondence of a fully linear elastic unloading and the residual strain upon unloading at zero stress. The values of σ_{PE} and ε_{PE} are summarized in Fig. 7c.

Fig. 4 a SEM micrograph of $Ni_{50.8}Ti$ powder. b Optical micrograph of the as-built LPBF produced NiTi showing the grains grown epitaxially toward the building direction. c and d SEM micrographs of the as-built LPBF produced NiTi highlighting the appearance of the melt pools and the cellular structure of the grains which is a consequence of the rapid solidification rate

IPF X **IPF Y** **Phase map**
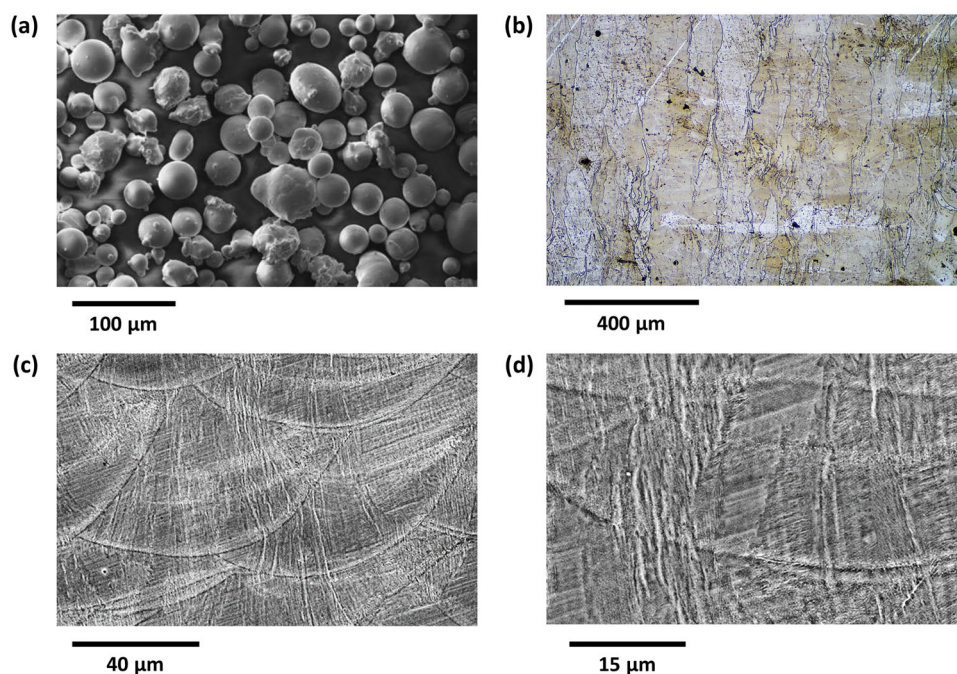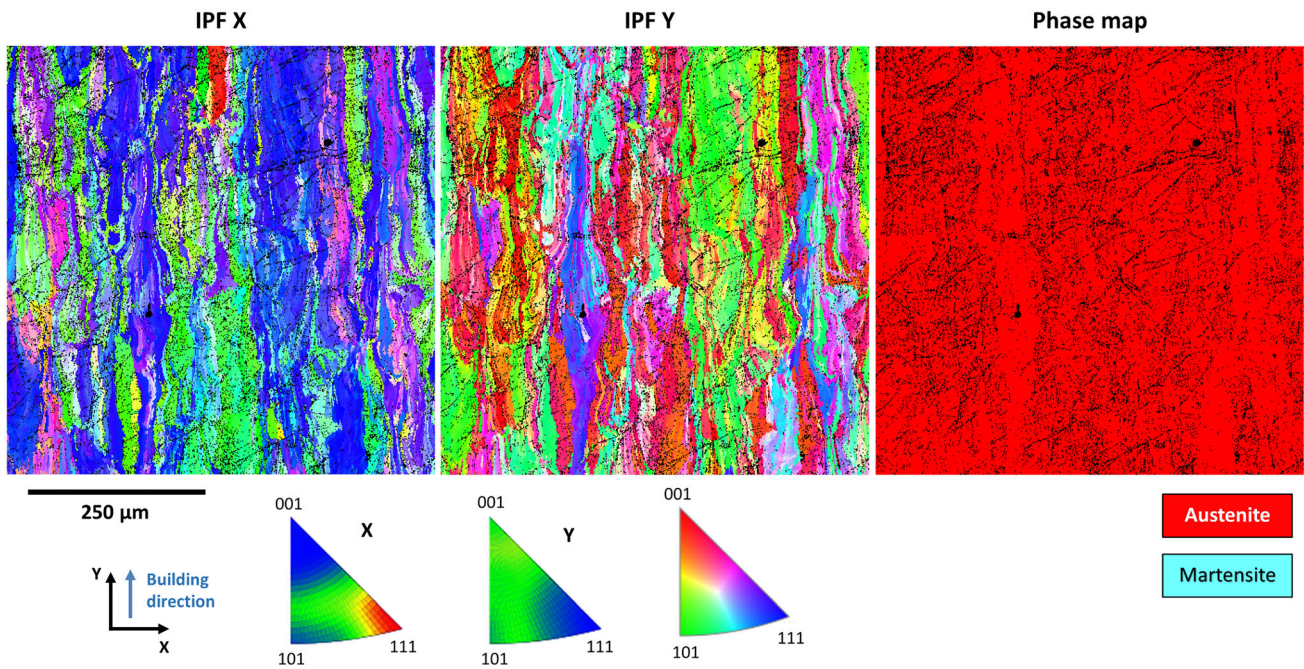
Fig. 5 The IPF map of the as-built NiTi in the *x* direction (perpendicular to the building direction), the IPF map in the *y* direction (parallel to the building direction), and the phase map

IPF Y **Phase map** **KAM map**
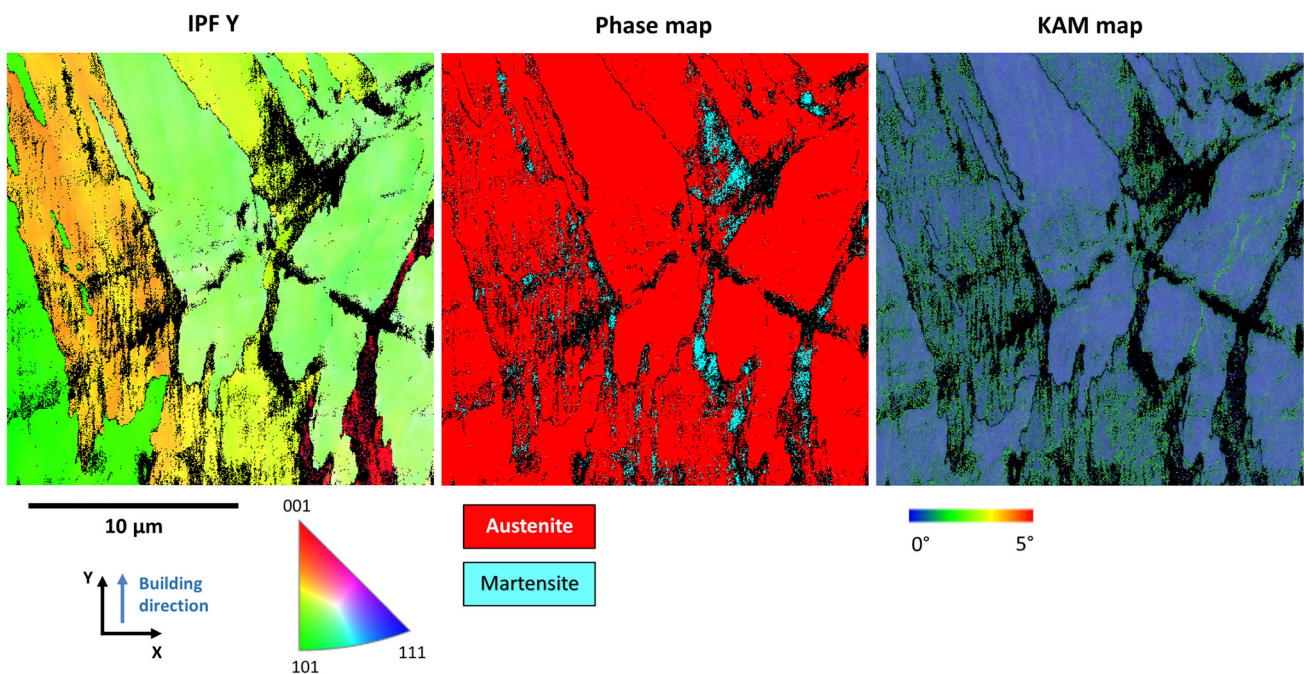
Fig. 6 The IPF map of the as-built NiTi in the *y* direction (corresponding to the building direction), the phase map, and the kernel average misorientation (KAM) map

The material exhibits pseudoelastic behavior at room temperature in all the testing conditions. The aged specimens show lower σ_{PE} with respect to the solution-treated specimen. This difference can be related to the increase in the transformation temperatures after the aging treatment [22]. The XRD analysis has shown that the aging treatment promotes the formation of Ni_4Ti_3 precipitates. It is widely recognized that the formation of such Ni-rich precipitates depletes Ni from the matrix, thus altering the Ni/Ti ratio and, therefore, modifying the transformation temperatures.
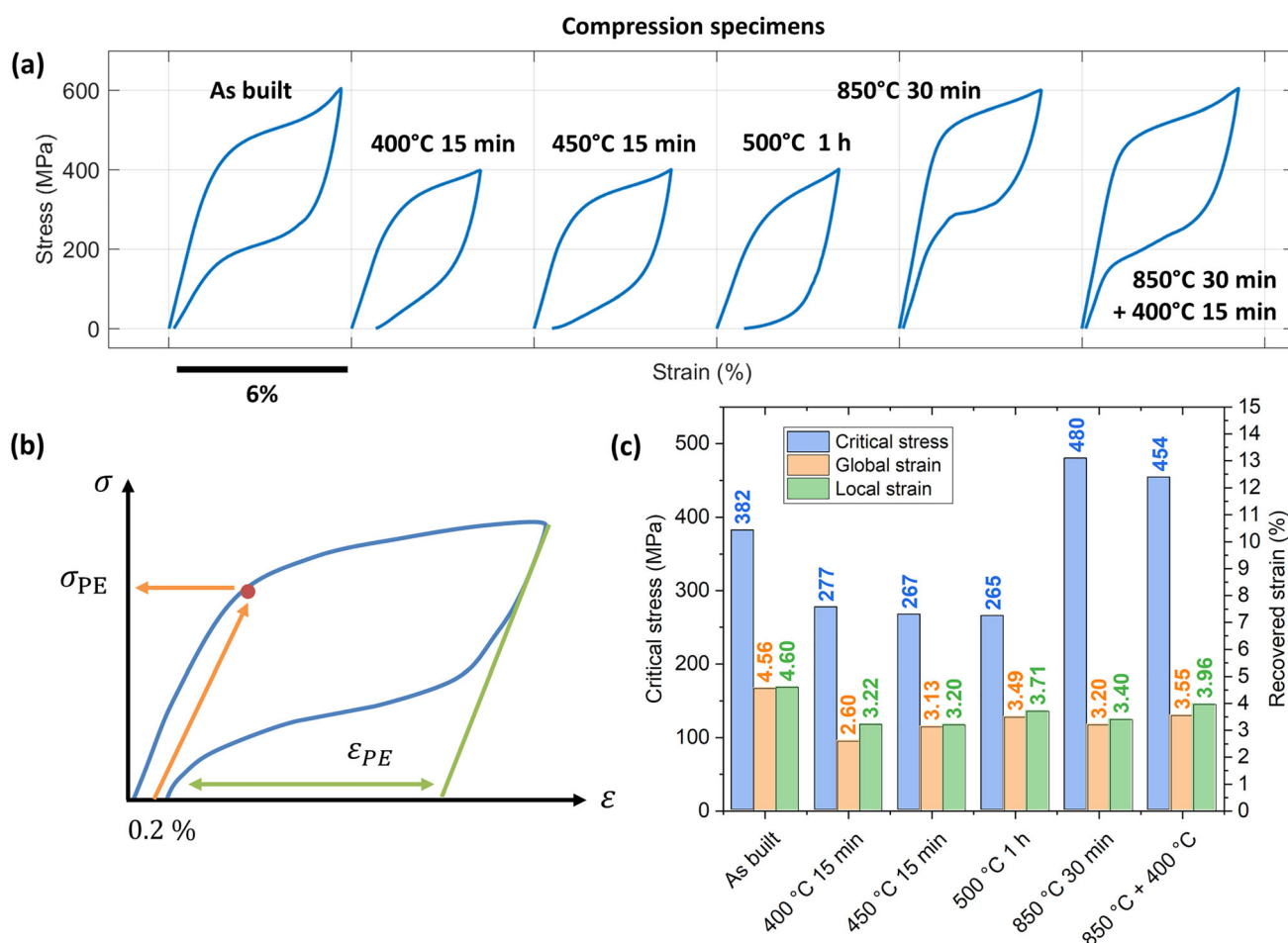
Fig. 7 a Stress–strain curves of the specimens tested in compression; the labels indicate the heat treatment conditions of each specimen. **b** A schematic illustrating the approximation used for the evaluation of the critical stress to induce the martensitic transformation σ_{PE} and the extent of recoverable strain due to the pseudoelastic effect (ε_{PE}). **c** Graphical summary of the main results obtained by compression testing of NiTi, in terms of critical stress and the extent of recovered strain both globally and locally

Moreover, the Ni-rich nano-sized coherent precipitates likely favor local stress intensification, leading the austenite to transform into martensite at lower values of nominal stress [55].

In Fig. 8, more details regarding the specimen aged at 450 °C and the specimen annealed at 850 °C are reported in terms of stress–strain curves and DIC strain maps. DIC contours allow to observe that the martensitic transformation does not occur with the same extent across the whole specimen. This supports the strong influence of the coarse-grained microstructure observed in the EBSD maps (Fig. 5).

The effect of cyclic loading was also investigated for the solution-treated specimen. The specimen was loaded up to 600 MPa and unloaded for 10 cycles. The stress–strain diagrams and DIC contours are reported in Fig. 8b. It is observed that, after cycling, the curve stabilizes and the unrecovered strain settles on 0.36%, which is a low value with respect to other results reported in the literature, since it is generally found that the curve of the 10th cycle in compression settles on a strain value higher than 2% [21, 22, 26, 28]. Moreover, the curve related to the 10th cycle is characterized by a reduced hysteresis and a lower value of recoverable strain with respect to the curve related to the 1st cycle (i.e., 2.46% with respect to 3.20%). This indicates that the pseudoelastic performances tend to degrade while increasing the number of loading cycles, as reported also in other studies on LPBF produced NiTi [21, 22, 26, 28]. This is consistent with the fact that the material is not trained [56], even though other works report a faster stabilization of the loading curve of LPBF produced NiTi with respect to the conventionally produced NiTi [13].

Tensile Behavior

The experimental results of the tensile tests are reported in Fig. 9a for the vertical specimens and in Fig. 9b for the
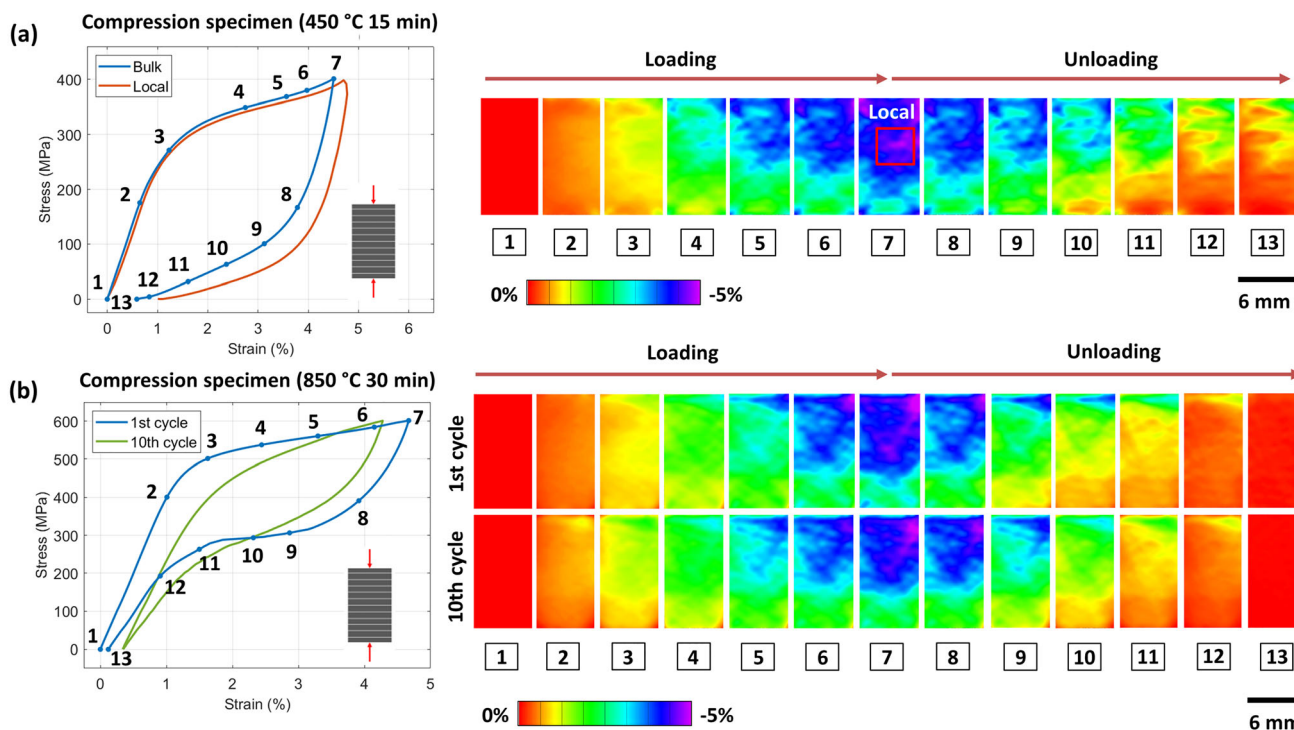
Fig. 8 Stress–strain curves and DIC contours for two compressive specimens: **a** the specimen aged at 450 °C and **b** the specimen annealed at 850 °C

horizontal specimens. The specimens were tested in different conditions: in the as-built state, after aging at 450 °C and after solution annealing at 850 °C followed by aging at 450 °C. The evaluated values of σ_{PE} and global and local

ε_{PE} for all the testing conditions are reported in Fig. 9c for both vertical and horizontal specimens.

The stress–strain diagram of the as-built vertical specimen shows a limited hysteresis and a very high value of
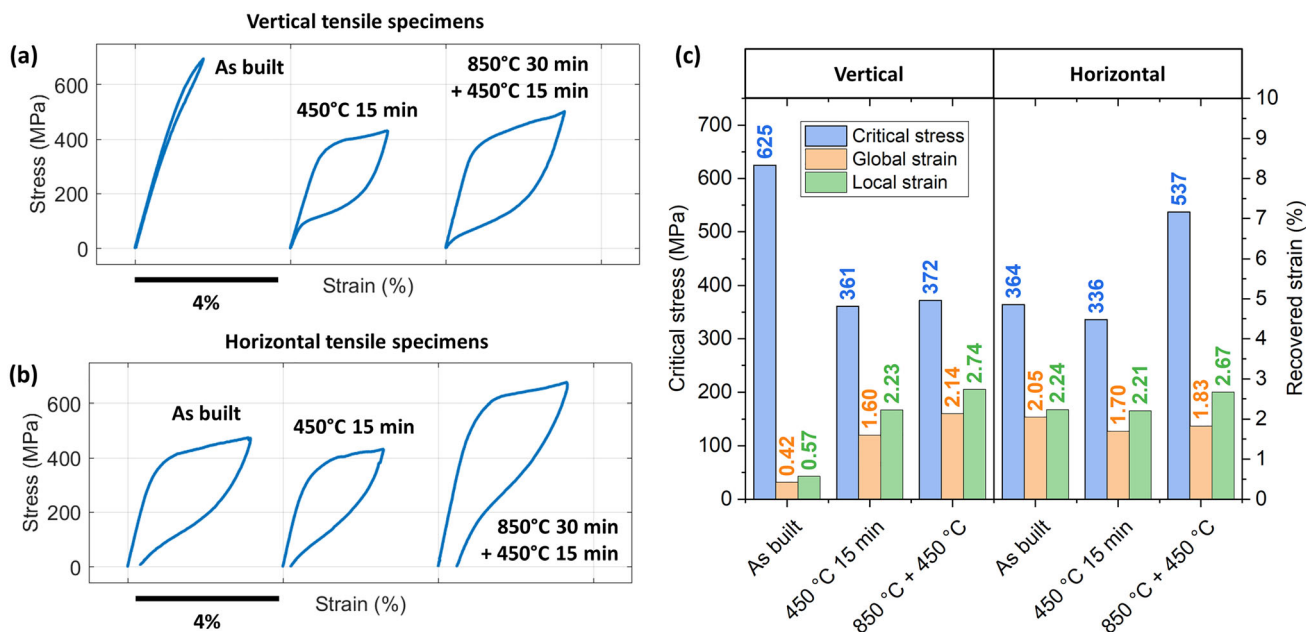
Fig. 9 Stress–strain curves for **a** the three vertical specimens and **b** the three horizontal specimens tested in tension; the labels indicate the testing conditions of each specimen, namely the heat treatments

performed. **c** Graphical summary of the main results obtained by tensile testing of NiTi, in terms of critical stress and the extent of recovered strain both globally and locally

critical stress (i.e., 625 °C). On the other hand, the aged specimens show a larger hysteresis and a lower value of critical stress (i.e., 361 MPa and 372 MPa). In all cases, a complete reverse phase transformation is observed, without irreversible strains. In Fig. 10a, more details about the behavior of the specimen aged at 450 °C are reported. The local stress–strain curve shows higher transformation strain values with respect to the global curve. In addition, DIC contours in Fig. 10a show that in the unloaded state, the specimen was able to recover almost all the strain across the whole surface.

For what concerns the horizontal specimens, the σ_{PE} was found to be 363 MPa in the as-built condition, in contrast to the value of 625 MPa found for the vertical specimen. Moreover, the horizontal specimen exhibits residual strains upon unloading, likely indicating the presence of a significant amount of martensite in the material. Such differences may be related also to the differences in the thermal histories. During the production of the horizontal specimens, larger areas are scanned in a given layer. Heat accumulation is more likely to occur during the scanning of horizontal specimens due to a prolonged laser interaction

A similar behavior is shown by the aged specimen. In this case, a residual deformation of 0.2% is reported. In this case, the specimen was heated up to 80 °C after unloading to induce the residual martensite to reversely transform into austenite. Then, the specimen was further analyzed with DIC, and the results are shown in Fig. 10b. It was found that the residual strains have almost totally recovered,

indicating that the transformation temperatures are slightly higher than that of testing. Finally, the solution-treated and aged specimen was deformed up to 3% and showed a residual deformation of 0.5%.

As a final remark, it is worth noting that the values of ε_{PE} reported in Fig. 9c allow to point out that the material in the heat-treated state shows higher local values of strain with respect to the global values, while in the as-built state the local and global behavior are almost the same. Moreover, Fig. 9c shows that the values of critical stress are not comparable between vertical and horizontal specimens, thus indicating a possible asymmetry in the mechanical behavior of the material depending on loading direction. The highest σ_{PE} was reported in the as-built condition (i.e., 625 MPa) for the vertical specimens and in the solution-treated and aged condition (i.e., 537 MPa) for the horizontal specimens. For both vertical and horizontal samples, the lowest σ_{PE} was shown after aging at 450 °C (i.e., 361 MPa and 336 MPa for the vertical and the horizontal specimens, respectively).

Conclusions

This work shows that LPBF is a process suitable to manufacture NiTi components with sound functional properties and provides valuable data that can be of interest for the exploitation of 3D printed NiTi pseudoelastic structures. The main findings can be summarized as follows:
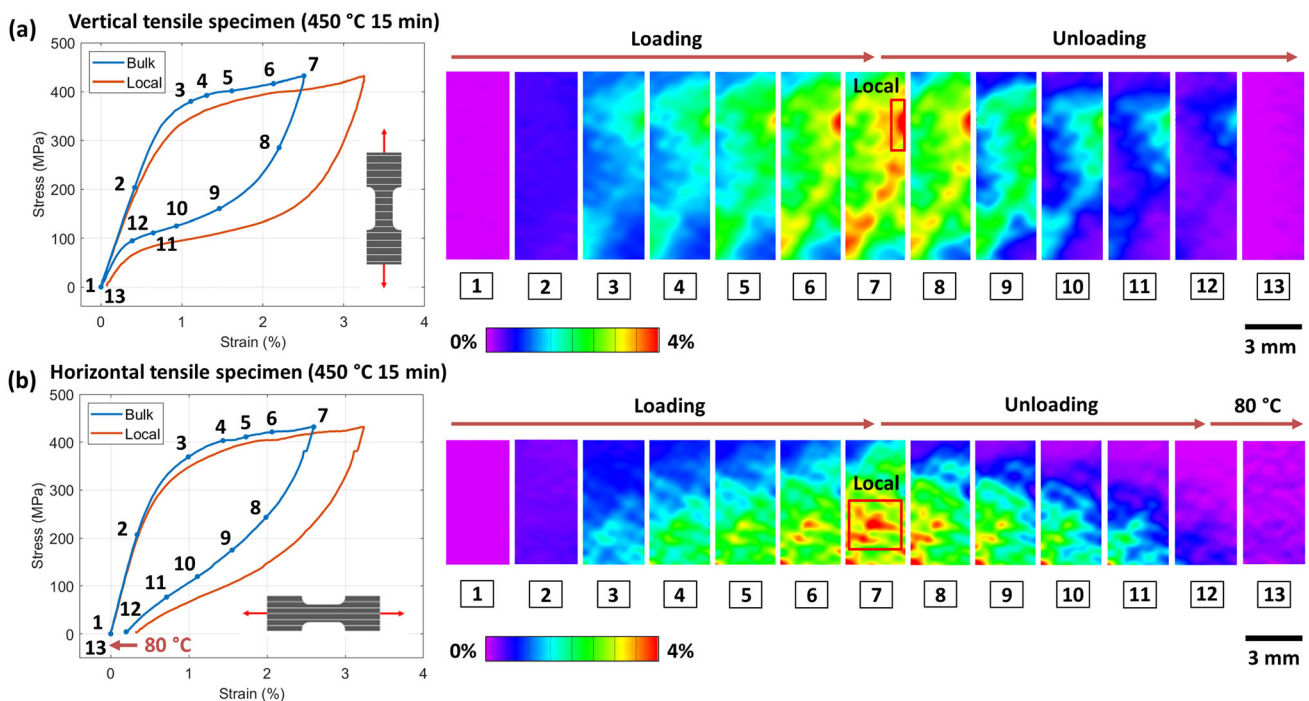
Fig. 10 Stress–strain curves and DIC contours for two tensile specimens aged at 450 °C: **a** the vertical and **b** the horizontal specimen

- The tested specimens exhibited pseudoelastic behavior at room temperature both in compression and in tension, in all the testing conditions.
- Post-process heat treatments were found to highly influence the pseudoelastic features of the material. Solution annealing at 850 °C increases the critical stress for the martensitic transformation, while aging between 400 and 500 °C decreases it.
- Regarding the mechanical behavior in compression, the highest values of recoverable strain were reported for the as-built condition (i.e., 4.56% globally and 4.60% locally). The highest value of critical stress (i.e., 480 MPa) was achieved by the specimen solution treated at 850 °C, while the lowest values (i.e., 277 ÷ 265 MPa) were shown by the specimens aged between 400 and 500 °C.
- The tensile specimens showed the highest strain recoverability after solution annealing at 850 °C followed by aging at 450 °C. The reported strain values were 2.14% globally and 2.74% locally for the vertical specimen, and 1.83% globally and 2.67% locally for the horizontal sample. Nevertheless, significant differences in the behavior of vertical and horizontal specimens can be pointed out, likely attributed to the different building orientations. The vertical specimen exhibited a lower value of critical stress (i.e., 372 MPa) with respect to the horizontal specimen (i.e., 537 MPa). Moreover, the horizontal specimen showed a residual strain of 0.5%, while the vertical specimen was able to recover completely.

References

1. Otsuka K, Ren X (2005) Physical metallurgy of Ti-Ni-based shape memory alloys. Progress Mater Sci 50(5):511–678. https://doi.org/10.1016/j.pmatsci.2004.10.001
2. Tušek J, Engelbrecht K, Mikkelsen LP, Pryds N (2015) Elastocaloric effect of Ni-Ti wire for application in a cooling device. J Appl Phys 117(12):124901. https://doi.org/10.1063/1.4913878
3. Cao Y et al (2020) Large tunable elastocaloric effect in additively manufactured Ni–Ti shape memory alloys. Acta Mater 194:178–189. https://doi.org/10.1016/j.actamat.2020.04.007
4. Van Humbeeck J (1999) Non-medical applications of shape memory alloys. Mater Sci Eng A 273–275:134–148. https://doi.org/10.1016/S0921-5093(99)00293-2
5. Machado LG, Savi MA (2003) Medical applications of shape memory alloys. Braz J Med Biol Res 36(6):683–691. https://doi.org/10.1590/S0100-879X2003000600001
6. Mohd Jani J, Leary M, Subic A, Gibson MA (2014) A review of shape memory alloy research, applications and opportunities. Mater Des 56:1078–1113. https://doi.org/10.1016/j.matdes.2013.11.084
7. Wadood A (2016) Brief overview on nitinol as biomaterial. Adv Mater Sci Eng. https://doi.org/10.1155/2016/4173138
8. Habijan T et al (2013) The biocompatibility of dense and porous Nickel-Titanium produced by selective laser melting. Mater Sci Eng C 33(1):419–426. https://doi.org/10.1016/j.msec.2012.09.008
9. Shaw JA, Churchill CB, Iadicola MA (2008) Tips and tricks for characterizing shape memory alloy wire: part 1-differential scanning calorimetry and basic phenomena. Exp Tech 32(5):55–62. https://doi.org/10.1111/j.1747-1567.2008.00410.x
10. Pelton AR, DiCello J, Miyazaki S (2000) "Optimisation of processing and properties of medical grade Nitinol wire. Min Invasive Therapy Allied Technol 9(2):107–118. https://doi.org/10.3109/13645700009063057
11. Kaynak Y, Tobe H, Noebe RD, Karaca HE, Jawahir IS (2014) The effects of machining on the microstructure and transformation behavior of NiTi Alloy. Scr Mater 74:60–63. https://doi.org/10.1016/j.scriptamat.2013.10.023
12. Hassan MR, Mehrpouya M, Dawood S (2014) Review of the machining difficulties of nickel-titanium based shape memory alloys. Appl Mech Mater 564:533–537. https://doi.org/10.4028/www.scientific.net/AMM.564.533
13. Elahinia M, Moghaddam NS, Andani MT, Amerinatanzi A, Bimber BA, Hamilton RF (2016) Fabrication of NiTi through additive manufacturing: a review. Progress Mater Sci 83:630–663. https://doi.org/10.1016/j.pmatsci.2016.08.001
14. Khoo ZX, Liu Y, An J, Chua CK, Shen YF, Kuo CN (2018) A review of selective laser melted NiTi shape memory alloy. Materials 11(4):519. https://doi.org/10.3390/ma11040519
15. Wang X, Kustov S, Van Humbeeck J (2018) A short review on the microstructure, transformation behavior and functional properties of NiTi shape memory alloys fabricated by selective laser melting. Materials 11(9):1683. https://doi.org/10.3390/ma11091683
16. Chekotu JC, Groarke R, O'Toole K, Brabazon D (2019) Advances in selective laser melting of Nitinol shape memory alloy part production. Materials 12(5):809. https://doi.org/10.3390/MA12050809
17. Alagha AN, Hussain S, Zaki W (2021) Additive manufacturing of shape memory alloys: A review with emphasis on powder bed

systems. Mater Des 204:109654. https://doi.org/10.1016/j.matdes.2021.109654

18. Li S, Hassanin H, Attallah MM, Adkins NJE, Essa K (2016) The development of TiNi-based negative Poisson's ratio structure using selective laser melting. Acta Mater 105:75–83. https://doi.org/10.1016/j.actamat.2015.12.017

19. Sharma N, Jangra KK, Raj T (2018) Fabrication of NiTi alloy: a review. Proc Inst Mech Eng Part L 232(3):250–269. https://doi.org/10.1177/1464420715622494

20. Khoo ZX et al (2015) 3D printing of smart materials: a review on recent progresses in 4D printing. Virtual Phys Prototyp 10(3):103–122. https://doi.org/10.1080/17452759.2015.1097054

21. Saedi S, Moghaddam NS, Amerinatanzi A, Elahinia M, Karaca HE (2018) On the effects of selective laser melting process parameters on microstructure and thermomechanical response of Ni-rich NiTi. Acta Mater 144:552–560. https://doi.org/10.1016/j.actamat.2017.10.072

22. Saedi S, Turabi AS, Andani MT, Haberland C, Karaca H, Elahinia M (2016) The influence of heat treatment on the thermomechanical response of Ni-rich NiTi alloys manufactured by selective laser melting. J Alloys Compd 677:204–210. https://doi.org/10.1016/j.jallcom.2016.03.161

23. Biffi CA, Tuissi A, Demir AG (2021) Martensitic transformation, microstructure and functional behavior of thin-walled Nitinol produced by micro laser metal wire deposition. J Mater Res Technol 12:2205–2215. https://doi.org/10.1016/j.jmrt.2021.03.108

24. Dadbakhsh S, Vrancken B, Kruth JP, Luyten J, Van Humbeeck J (2016) Texture and anisotropy in selective laser melting of NiTi alloy. Mater Sci Eng A 650:225–232. https://doi.org/10.1016/j.msea.2015.10.032

25. Maffia S et al (2021) Selective laser melting of NiTi stents with open-cell and variable diameter. Smart Mater Struct 30(10):105010. https://doi.org/10.1088/1361-665X/ac1908

26. Moghaddam NS et al (2019) Achieving superelasticity in additively manufactured NiTi in compression without post-process heat treatment. Sci Rep 9(1):1–11. https://doi.org/10.1038/s41598-018-36641-4

27. Dadbakhsh S, Speirs M, Kruth JP, Schrooten J, Luyten J, Van Humbeeck J (2014) Effect of SLM parameters on transformation temperatures of shape memory nickel titanium parts. Adv Eng Mater 16(9):1140–1146. https://doi.org/10.1002/adem.201300558

28. Haberland C, Elahinia M, Walker JM, Meier H, Frenzel J (2014) On the development of high quality NiTi shape memory and pseudoelastic parts by additive manufacturing. Smart Mater Struct. https://doi.org/10.1088/0964-1726/23/10/104002

29. Walker J, Andani MT, Haberland C, Elahinia M (2014) Additive manufacturing of Nitinol shape memory alloys to overcome challenges in conventional Nitinol fabrication. In: ASME International Mechanical Engineering Congress and Exposition, Proceedings (IMECE), vol. 2A, doi: https://doi.org/10.1115/IMECE2014-40432.

30. Dadbakhsh S, Speirs M, Van Humbeeck J, Kruth JP (2016) Laser additive manufacturing of bulk and porous shape-memory NiTi alloys: from processes to potential biomedical applications. MRS Bull 41(10):765–774. https://doi.org/10.1557/mrs.2016.209

31. Saedi S, Turabi AS, Andani MT, Moghaddam NS, Elahinia M, Karaca HE (2017) Texture, aging, and superelasticity of selective laser melting fabricated Ni-rich NiTi alloys. Mater Sci Eng A 686:1–10. https://doi.org/10.1016/j.msea.2017.01.008

32. Biffi CA, Bassani P, Fiocchi J, Tuissi A (2020) Microstructural and mechanical response of niti lattice 3d structure produced by selective laser melting. Metals (Basel) 10(6):1–9. https://doi.org/10.3390/met10060814

33. Biffi CA, Fiocchi J, Valenza F, Bassani P, Tuissi A (2020) Selective laser melting of NiTi shape memory alloy: processability, microstructure, and superelasticity. Shape Mem Superelasticity 6(3):342–353. https://doi.org/10.1007/s40830-020-00298-8

34. Chen X, Liu K, Guo W, Gangil N, Siddiquee AN, Konovalov S (2019) The fabrication of NiTi shape memory alloy by selective laser melting: a review. Rapid Prototyp J 25(8):1421–1432. https://doi.org/10.1108/RPJ-11-2018-0292

35. Frenzel J, George EP, Dlouhy A, Somsen C, Wagner MFX, Eggeler G (2010) Influence of Ni on martensitic phase transformations in NiTi shape memory alloys. Acta Mater 58(9):3444–3458. https://doi.org/10.1016/j.actamat.2010.02.019

36. Bormann T, Schumacher R, Müller B, Mertmann M, De Wild M (2012) Tailoring selective laser melting process parameters for niti implants. J Mater Eng Perform 21(12):2519–2524. https://doi.org/10.1007/s11665-012-0318-9

37. Bormann T, Müller B, Schinhammer M, Kessler A, Thalmann P, De Wild M (2014) Microstructure of selective laser melted nickel-titanium. Mater Charact 94:189–202. https://doi.org/10.1016/j.matchar.2014.05.017

38. Parvizi S, Hashemi SM, Asgarinia F, Nematollahi M, Elahinia M (2021) Effective parameters on the final properties of NiTi-based alloys manufactured by powder metallurgy methods: A review. Progress Mater Sci 117:100739. https://doi.org/10.1016/j.pmatsci.2020.100739

39. Haberland C, Meier H, Frenzel J (2012) On the properties of Ni-rich NiTi shape memory parts produced by selective laser melting. in ASME 2012 Conference on Smart Materials, Adaptive Structures and Intelligent Systems, SMASIS 2012, vol 1, pp 97–104, doi: https://doi.org/10.1115/SMASIS2012-8040.

40. Nematollahi M et al (2021) Building orientation-structure-property in laser powder bed fusion of NiTi shape memory alloy. J Alloys Compd 873:159791. https://doi.org/10.1016/j.jallcom.2021.159791

41. Lu HZ et al (2021) Stable tensile recovery strain induced by a Ni4Ti3 nanoprecipitate in a Ni50.4Ti49.6 shape memory alloy fabricated via selective laser melting. Acta Mater 219:117261. https://doi.org/10.1016/j.actamat.2021.117261

42. Xue L et al (2022) Laser powder bed fusion of defect-free NiTi Shape memory alloy parts with superior tensile superelasticity. Acta Mater 229:117781. https://doi.org/10.1016/j.actamat.2022.117781

43. Li B et al (2021) Solidification characterization and its correlation with the mechanical properties and functional response of NiTi shape memory alloy manufactured by electron beam freeform fabrication. Addit Manuf 48:102468. https://doi.org/10.1016/j.addma.2021.102468

44. Huang K et al (2022) High superelasticity niti fabricated by cold metal transfer based wire arc additive manufacturing. SSRN Electron J. https://doi.org/10.2139/ssrn.4004796

45. Kok Y et al (2018) Anisotropy and heterogeneity of microstructure and mechanical properties in metal additive manufacturing: a critical review. Mater Des 139:565–586. https://doi.org/10.1016/j.matdes.2017.11.021

46. Sehitoglu H et al (2003) Detwinning in NiTi alloys. Metall Mater Trans A 34(1):5–13. https://doi.org/10.1007/s11661-003-0203-0

47. Moghaddam NS et al (2018) Anisotropic tensile and actuation properties of NiTi fabricated with selective laser melting. Mater Sci Eng A 724:220–230. https://doi.org/10.1016/j.msea.2018.03.072

48. Gall K, Sehitoglu H, Anderson R, Karaman I, Chumlyakov YI, Kireeva IV (2001) On the mechanical behavior of single crystal NiTi shape memory alloys and related polycrystalline phenomenon. Mater Sci Eng A 317(1–2):85–92. https://doi.org/10.1016/S0921-5093(01)01183-2

49. Hamilton RF, Bimber BA, Palmer TA (2018) Correlating microstructure and superelasticity of directed energy deposition additive manufactured Ni-rich NiTi alloys. J Alloys Compd 739:712–722. https://doi.org/10.1016/j.jallcom.2017.12.270

50. Undisz A, Rettenmayr M, Wilke M, Spieβ L (2009) Non-martensitic Needle-like Structures on Ni-Ti Alloys - Occurrence and Origin," in *European Symposium on Martensitic Transformations*, p. 02034, doi: https://doi.org/10.1051/esomat/200902034.

51. Khalil-Allafi J, Eggeler G, Schmahl WW, Sheptyakov D (2006) Quantitative phase analysis in microstructures which display multiple step martensitic transformations in Ni-rich NiTi shape memory alloys. Mater Sci Eng A 438–440:593–596. https://doi.org/10.1016/j.msea.2006.02.143

52. Jiang SY, Zhang YQ, Zhao YN, Liu SW, Hu L, Zhao CZ (2015) Influence of Ni4Ti3 precipitates on phase transformation of NiTi shape memory alloy. Trans Nonferrous Met Soc China 25(12):4063–4071. https://doi.org/10.1016/S1003-6326(15)64056-0

53. Khaleghi F, Khalil-Allafi J, Abbasi-Chianeh V, Noori S (2013) Effect of short-time annealing treatment on the superelastic behavior of cold drawn Ni-rich NiTi shape memory wires. J Alloys Compd 554:32–38. https://doi.org/10.1016/j.jallcom.2012.11.183

54. Saedi S, Turabi AS, Andani MT, Haberland C, Elahinia M, Karaca H (2016) Thermomechanical characterization of Ni-rich NiTi fabricated by selective laser melting. Smart Mater Struct 25(3):035005. https://doi.org/10.1088/0964-1726/25/3/035005

55. Chowdhury P, Patriarca L, Ren G, Sehitoglu H (2016) Molecular dynamics modeling of NiTi superelasticity in presence of nano-precipitates. Int J Plast 81:152–167. https://doi.org/10.1016/j.ijplas.2016.01.011

56. Nemat-Nasser S, Guo WG (2006) Superelastic and cyclic response of NiTi SMA at various strain rates and temperatures. Mech Mater 38(5–6):463–474. https://doi.org/10.1016/j.mechmat.2005.07.004